Materiales de Construcción 75 (358)
April-June 2025, e372
ISSN-L: 0465-2746, eISSN: 1988-3226
https://doi.org/10.3989/mc.2025.397024

Evaluation of the physical sulfate attack resistance of lightweight concrete with thermally expanded clay

P. A. López[a,b], J. I. Tobón[a], J. F. Arango-L[c]

a. Cement and Construction Materials Research Group. Materials and Minerals Department, Facultad de Minas, Universidad Nacional de Colombia (Medellin, Antioquia, Colombia)
b. Sumicol Corona, (Medellin, Antioquia, Colombia)
c. Cemento Alión, (Medellin, Antioquia, Colombia)
✉: paalopezsa@unal.edu.co

Received 18 October 2024
Accepted 7 February 2025
Available on line 27 Ausgust 2025

ABSTRACT: The phenomenon of physical sulfate attack (PSA) is scarcely studied, particularly in lightweight concrete (LWC) comprising thermally expanded clay aggregate (TECA). The mass change and visual appearance as well as other physical properties, such as the compressive strength, equilibrium density, sorptivity, open porosity, and water conductivity, of the concrete samples were evaluated. Additionally, characterization techniques, such as X-ray fluorescence, X-ray diffraction, and scanning electron microscopy, were employed to identify the formed substances after sulfate exposition. Our results revealed a dual attack, by PSA and the chemical reactions that form the sulfates, in LWC and normal weight concrete (NWC). The higher the TECA content, the lower the compressive strength and the relative PSA resistance. However, with the improvement of cement paste, the aforementioned result was reversed. The relatively closed internal alveolar structure present in TECA did not host sodium sulfate crystals or other substances.

KEY WORDS: Concrete; Lightweight concrete; Sodium sulfate attack; Physical sulfate damage; Dual sulfate attack.

Citation/Citar como: Lopez PA, Tobón JI, Arango-L JF. 2025. Evaluation of the physical sulfate attack resistance of lightweight concrete with thermally expanded clay. Mater. Construcc. 75(358):e372. https://doi.org/10.3989/mc.2024.397024.

RESUMEN: *Evaluación de la resistencia al ataque físico por sulfatos de un hormigón ligero con arcilla expandida.* El fenómeno de ataque físico por sulfatos (AFS) ha sido escasamente estudiado, especialmente para hormigones ligeros con áridos de arcilla térmicamente expandida (AEx). Se evaluaron cambio de masa, apariencia visual, resistencia a compresión, densidad de equilibrio, sorción, porosidad abierta y conductividad hidráulica, de muestras de hormigón. Además, se emplearon técnicas de caracterización, como fluorescencia de rayos X, difracción de rayos X y microscopía electrónica de barrido, para identificar las sustancias formadas después de exposición a sulfatos. Nuestros resultados muestran que durante el AFS ocurre un ataque dual, por AFS y por reacciones químicas en el hormigón ligero (CL) y en el de peso normal (CN). A mayor cantidad de AEx disminuye la resistencia a la compresión y al AFS. Pero, con la mejora de la pasta de cemento, el resultado se revirtió. La estructura alveolar interna relativamente cerrada de TECA no albergaba cristales de sulfato de sodio ni otras sustancias.

PALABRAS CLAVE: Hormigón; Hormigón ligero; Ataque por sulfato de sodio; Daño físico por sulfato; Ataque dual de sulfato.

1. INTRODUCTION

Chemical sulfate attack has been extensively studied, as sulfates react with cement to form products that cause concrete damage (1). However, negligible attention has been devoted to the physical damage related to the crystallization and recrystallization of sodium sulfate or magnesium sulfate interacting with the concrete, which is also known as physical sulfate attack (PSA). Under service conditions, sulfates generally originate from external sources, and the sulfate-containing solution ingresses into the concrete mainly via absorption, hydraulic conductivity, and diffusion. The higher the concentration of sodium sulfate or magnesium sulfate, the more severe the concrete damage (2). However, PSA requires environmental conditions such as wet/dry cycles and temperature changes as well as the crystallization kinetics that promote crystal formation (2). Concrete completely submerged in sodium sulfate media will develop chemical sulfate attack in addition to PSA during long-term exposure. Several test procedures, such as ASTM C1012, employ 5% sodium sulfate solution and a temperature of 23ºC with long testing times, up to 18 months, and the temperature and concentration of the liquid sodium solution are low, based on the phase diagram, preventing PSA (3). In pure PSA, the sodium sulfate solution migrates from the concrete surface through permeable pores and undergoes phase changes between mirabilite and thenardite, with associated volume changes (4), presumably inducing concrete "fatigue" similar to salt scaling upon freeze/thaw exposure. Hence, the interconnection of pores plays a substantial role in the development of PSA, and the volume changes during crystallization and recrystallization cause stresses surmounting the strength resistance of the concrete, leading to its deterioration with cracking, spalling, scaling, and mass loss (5-8). Several supplementary cementitious materials (SCMs) contribute to the mitigation of chemical sulfate attack and PSA (6, 9-12). Specifically, metakaolin (MK) contributes to the improvement of the cementitious paste and PSA resistance (13). ACI 201.2R-16, Guide to Durable Concrete, proposes the use of water/cement (*w/c*) ratios of <0.45 (14, 15) as a prescriptive measure. Although the use of high-sulfate-resistance (HS) cement mitigates chemical sulfate attack, it is not effective in alleviating PSA, as different damage mechanisms are involved.

The deterioration of concrete due to PSA has been practically observed in various structures exposed to wetting and drying cycles as well as temperature changes (16). Researchers have attempted to replicate the PSA phenomenon in the laboratory (12, 17, 8, 18). However, a widely accepted standard has not been established for testing the PSA resistance. In certain cases, tests are conducted via the wetting and drying cycles of the concrete samples exposed to sulfates, either through partial immersion or complete submersion with temperature variations (7, 17, 19). In this study, immersed concrete bars were evaluated in a 30% wt. sodium sulfate solution to quantify the variations in mass and record the notable physical changes based on the method proposed by Zhutovsky and Hooton (8, 20), hereinafter referred as the ZH90 method.

The PSA resistance of normal-weight concrete (NWC) has not been well studied. Furthermore, the understanding of PSA on lightweight concrete (LWC) comprising thermally expanded clay aggregate (TECA) remains lacking. In general, the use of LWC reduces the size of the foundation of buildings because of a decreased structural dead load and lowers the quantity of reinforcing steel required while providing increased thermal comfort and good structural and seismic characteristics, contributing to sustainable construction (21). However, LWC comprising TECA would behave as a material vulnerable to sulfate attack owing to its alveolar structure. Based on the aforementioned discussion, this study aims to investigate the behavior of LWC comprising TECA under accelerated PSA induced by temperature variations in a sodium sulfate solution. Concrete samples with different proportions of TECA were tested, and their porosity, hydraulic conductivity, and sorptivity values were compared.

The objective of this study is to determine the effects of the LWC pore structure on PSA damage. Furthermore, this study is expected to provide guidelines for the future utilization of LWC. From a scientific perspective, this study intends to reveal the causes and mechanism of the PSA phenomenon when the concrete contains TECA. Additionally, this study aims to contribute to the development of concrete technology and offers insights for generalizing the use of TECA in the production of LWC resistant to sulfate-rich environments.

2. MATERIALS AND METHODS

2.1. Methods

The aggregates used were characterized based on the ASTM C 33 specifications for normal-weight aggregate (NWA) and ASTM C 330 for TECA. A reference mix design for the NWA 51.5 MPa concrete strength was adopted as the reference mix (F0G0). The LWC samples were obtained by progressively replacing NWA with TECA in proportions of 30%, 60%, and 100% of the total aggregate volume while maintaining the same amount of cement. To test the effects on PSA resistance of the *w/cm* ratio, two ratios, namely, 0.49 and 0.45, were

used. The compressive strength parameters and equilibrium density were evaluated based on ASTM C39 and ASTM C567 standards. In this procedure, all the TECA replacements exceeded 18.8 MPa concrete strength, and the maximum equilibrium density was 1920 kg/m³. Another set of samples was obtained utilizing an improved concrete paste comprising 10% MK and by reducing the *w/cm* ratio to 0.45. MK reacts with portlandite to form C–S–H and C–A–S–H, resulting in the porosity refinement of the cementitious paste. Compressive strength was measured using cylindrical concrete samples with the dimensions of 150 mm × 300 mm, following the respective testing standards. The compressive strength tests were conducted at 7 and 28 d. Several samples were selected to study the effects of TECA in comparison with those of NWA on parameters such as water permeability, open porosity (ASTM C642), and sorptivity (ASTM C1585). Cylindrical concrete specimens with the dimensions of 100 × 200 mm were prepared for this purpose and were cured in water at 23ºC ± 2°C.

The PSA resistance was evaluated by measuring the mass change of the concrete bars with the dimensions of 40 × 40 × 160 mm using the ZH90 method with certain practical modifications. Briefly, the concrete specimens were immersed in a sodium sulfate solution with a 30% wt. concentration. The test involved 90 cycles of thermal variations, each lasting for 24 h, within a target temperature range of 4ºC ± 1ºC to 32ºC ± 2°C, with a temperature change rate of approximately 2°C/h. The mass change was measured at every seven cycles, i.e., weekly. At the end of the test, the attacked samples were observed using an optical microscope (OLYMPUS 8Zx18) and a scanning electron microscopy (SEM) system (Phenom PROX), following the ASTM C856 method. The concrete samples were observed at the magnifications that enabled the identification of aggregates, cementitious paste, interface-transition-zone (ITZ) configuration, and formed minerals as well as the respective textures and morphologies; their chemical composition was analyzed using energy-dispersive spectroscopy (EDS). To corroborate the microscopic observations, X-ray fluorescence (XRF) analysis was conducted to confirm the formation of mineral phases.

The ZH90 method was modified as follows:

• Concrete was used instead of mortars. The maximum nominal size of the aggregate used was 12 mm to obtain specimens with thickness exceeding the maximum aggregate size by three times.

• Each mix was produced using a portable mixer (Rubimix-9). Three specimens of each mix were cast and compacted using a tamper (ASTM C109) and a rubber mallet.

• Because the hydrated lime used in standard curing might chemically react with sulfate during the PSA test, the curing water used for the bars was not added with lime. A limited water:specimen volume ratio of 2:1 was used to prevent excessive lixiviation. After curing, one specimen, F0G0-1, was maintained in the as-obtained state as a reference, while the other two specimens were used for the PSA test. The saturated-surface-dry mass of each specimen was measured at the end of curing and after each PSA cycle.

• The specimens were placed into airtight containers stacked in rows separated by a rigid 4-mm-thick plastic mesh to facilitate contact with the solution around all the specimen faces.

• A temperature-programable water bath, which was equipped with a pump to recirculate the water around the airtight containers for uniform thermal exposition, was used.

• An additional temperature logger was placed in contact with the solution inside the airtight container to assess its thermal cycles.

• The airtight containers were placed in the temperature bath. The water level in the bath was maintained at approximately the same position as that of the sulfate solution level inside the airtight containers.

• Each thermal cycles lasted for 24 h, with temperature variations between 4ºC ± 1ºC and 32ºC ± 2°C, at a temperature change rate of 2°C/h. The increase in the upper target temperature might enable the thermodynamic conditions for facilitating the phase changes between mirabilite and sodium sulfate solution, based on the real temperature variations reported for the ZH90 method (8, 12, 20).

• After every seven cycles, the specimens were removed from the airtight containers and brushed. Thereafter, they were conditioned to attain a saturated-surface-dry condition and weekly weighed for determining the mass change.

The flowchart depicted in Figure 1 summarizes the modified ZH90 method used for PSA testing.

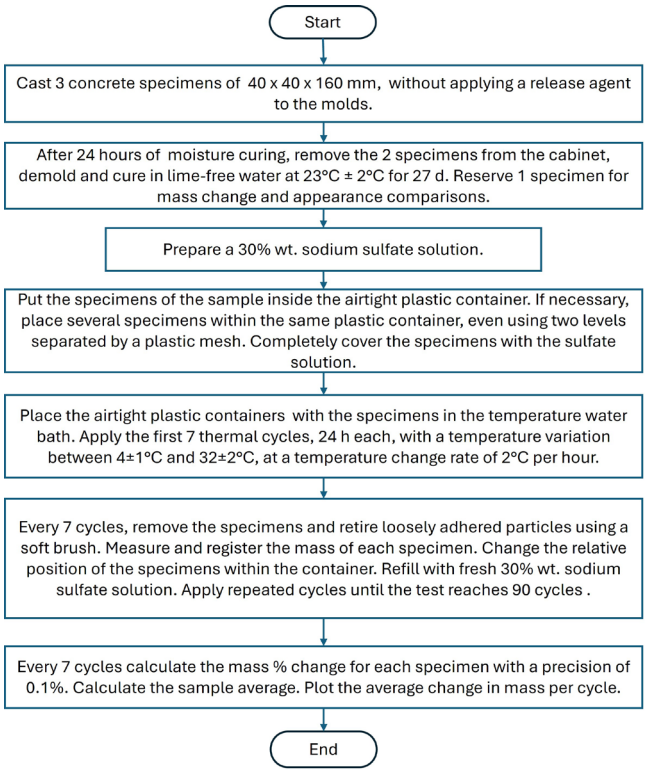

Figure 1. Flowchart of the modified ZH90 method for PSA testing.

2.2. Materials and characterization

The chemical characteristics of the materials used are detailed in Table 1. ASTM C1157 high-early-strength hydraulic cement (HE) was used in combination with a calcite filler. The chemical composition of each material was determined via XRF using a Panalytical Axios mineral instrument. Additionally, a 30% wt. sodium sulfate solution (99.0% purity) was used for PSA tests, and the solution was prepared using deionized water. Tables 2 and 3 list the physical properties of the aggregates employed, as determined using ASTM C127, ASTM C128, and ASTM C136 standards.

Table 1. Chemical composition of the aggregates, MK, and cement.

	NWA	TECA	MK	HE Cement
Silicon Oxide (SiO_2)	53.5	65.6	55.8	21.2
Aluminum oxide (Al_2O_3)	17.9	18.1	39.7	4.68
Iron oxide (Fe_2O_3)	8.54	10.0	1.32	3.1
Titanium oxide (TiO_2)	0.68	0.9	1.3	-
Magnesium oxide (MgO)	4.01	2.5	0.04	2.33
Calcium oxide (CaO)	9.24	0.4	0.07	60.5
Sodium oxide (Na_2O)	1.89	0.6	0.01	0.45
Potassium oxide (K_2O)	0.26	1.6	0.14	0.68
Phosphorus (P_2O_5)	0.09	0.1	0.03	-
Sulfur oxide (SO_3)	-	-	-	2.93
Ignition losses at 1000 ºC	3.9	0.3	2.05	4.16

Table 2. Physical properties of the aggregates.

	Bulk density (kg/m³)	Apparent density (g/cm³)	Absorption (%)
Sand 4.75 mm (fine)	1660	2.79	1.2
Gravel 9.5mm (coarse)	1600	2.73	0.69
TEC 6 to 12 mm	450	0.75	26.65
TEC < 6 mm	600	0.90	25.9

Table 3. Aggregate gradiation.

SIEVE	PERCENTAGE PASSING			
SIZE (mm)	Gravel 9.5mm (coarse)	Sand 4.75 mm (fine)	TEC 6 to 12 mm	TEC < 6 mm
12.7	100	100	99.3	100
9.51	97	100	33.9	100
4.76	28	100	0.8	91.1
2.38	10	90.1	0.6	-
1.19	3	64.1	0	51.3
0.595	0,6	41.5	0	-
0.297	0,0	29.6	0	18.4
0.149	0,0	19.5	0	12.8

X-ray diffraction (XRD) was conducted using a Panalytical Empyrean instrument in a 2θ range of 2.5°–70° with a step size of 0.26°. The accumulation time was 90 s/step, and a copper source was employed. The results obtained for MK are displayed in Figure 2. The amorphous content and other unidentified materials were quantified using an indirect method with the addition of a 20% internal standard (rutile). The amorphous content in MK was determined as 71%–75%, with the quartz content ranging from 13% to 17%. From Figure 3, in sand, the quartz and plagioclase contents are 25%–30% and 15%–20%, respectively, and the content of vermiculite and/or chlorite and/or smectite is 14%–18%, in addition to the presence of other components. Figure 4 illustrates the XRD results of TECA, revealing that the amorphous content is predominant, ranging from 43% to 48%, and the quartz content is 28%–33%, among the other constituents.

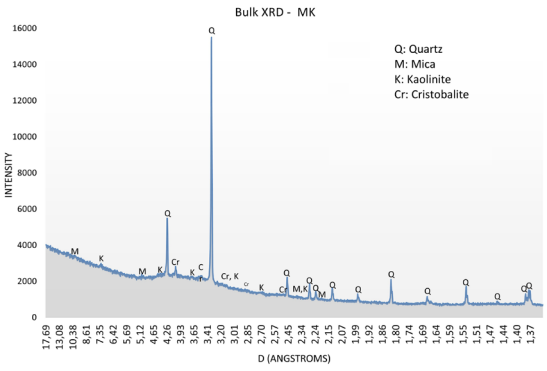

Figure 2. X-ray diffractrogram of MK.

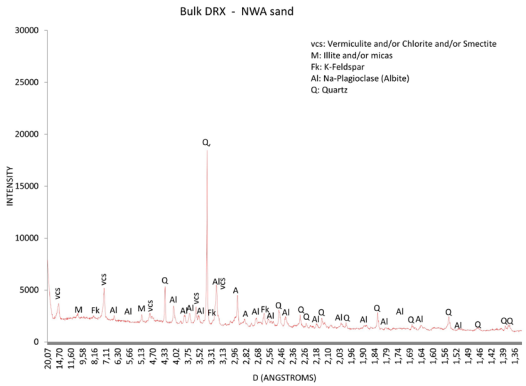

Figure 3. X-ray diffractrogram of NWA sand.

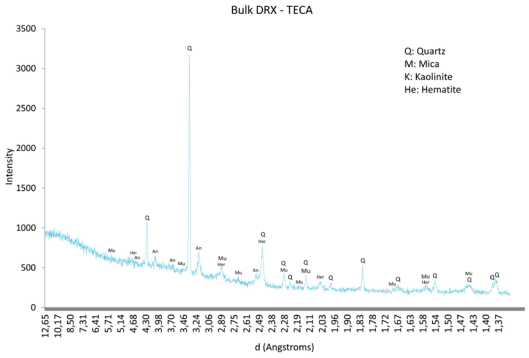

Figure 4. X-ray diffractrogram of TECA.

The water penetration depth was determined as stated by NTC 4483, using a pressure of 0.5 MPa for 4 d. The open porosity was determined using ASTM C673. Sorptivity was measured based on ASTM C1585.

2.3. Specimen preparation

One set of concrete samples was prepared with a *w/cm* ratio of 0.49. Bars samples with the dimensions of 40 × 40 × 160 mm were cast for the PSA test. Cylindrical samples with the dimensions of 150 mm × 300 mm were used for testing the compressive strength and equilibrium density, whereas cylinders with the dimensions of 100 × 200 mm were employed for measuring the water sorptivity and permeability. All the specimens were demolded after 24 h and subsequently cured in water for 27 days at 23ºC ± 2°C. The concrete mix proportions are listed in Table 4. Mix identification: G denotes coarse aggregate, and F corresponds to fine aggregate, followed by a number indicating the respective percentage volume replacement of NWA by TECA. For the mixtures containing 10 wt % MK, the identification was prefixed accordingly. Furthermore, another set of samples was prepared with a *w/cm* ratio of 0.45, and the aforementioned prefix convention was used. The 10 wt% MK replacement was selected for the PSA tests, as it was determined as the optimum content that facilitated a low hydraulic conductivity in NWC, based on multiple previous tests.

Table 4. Mix design.

Material	G0F0	G100F0	G100F30	G100F60	G100F100	MKG0F0	MKG100F30	MKG100F100	0.45G100F30
w/cm	0.49	0.49	0.49	0.49	0.49	0.49	0.49	0.49	0.45
Water (L)	210	210	210	210	210	210	210	210	195
Cement HE (kg)	430	430	430	430	430	387	387	387	430
Metakaolin (kg)	-	-	-	-	-	43	43	43	0
Fine aggregate < 4.75 mm (kg)	1083.8	1083.8	758.7	433.5	0.00	1080.1	756.1	0.00	777.4
Coarse aggregate > 9.5 mm (kg)	722.5	0.00	0.00	0.00	0.00	720.1	-	-	-
TECA 6 to 12 mm (kg)	-	203.2	203.2	203.2	203.2	-	202.5	202.5	208.2
TECA < 6 mm (kg)	-	0.00	117.5	235.04	391.7	-	117.1	390.4	120.4
Water-reducing, high range admixtures (kg)	2.58	2.58	2.58	2.58	2.58	2.58	2.58	2.58	2.58

3. RESULTS AND DISCUSSION

3.1. Compressive strength and equilibrium density

Figure 5 depicts the compressive strength of the concrete samples, in which NWA is replaced by TECA, with a *w/cm* ratio of 0.49. The compressive strength of the LWC samples comprising TECA was lower than that of the concrete without aggregate replacement (G0F0). The LWC samples demonstrated an equilibrium density (ASTM C567) of <1920 kg/m^3. When the volume replacement of NWA by TECA increased, the compressive strength decreased, as expected. Furthermore, this phenomenon is observed in LWC with an improved paste performance, as presented in Figures 5 and 6. The G100F30 sample is notable, as its compressive strength increased from 22.02 to 26.41 MPa with the use of 10% MK (Figures 5, 6, and 7). In both cases for LWC, an exponential relation is observed between the compressive strength and oven-dry and equilibrium densities (ASTM 567), as depicted in Figure 8, which is consistent with the previous literature reports (22-24). In the present study, this result is relevant for the interpretation of the PSA resistance, as the tested samples exhibit different compressive strengths with increasing TECA content. The samples with a higher compressive strength are expected to better withstand the crystallization pressure, leading to less damage.

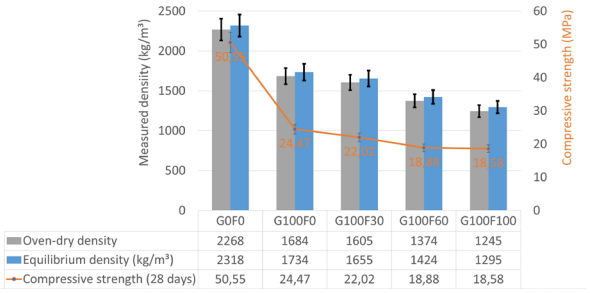

Figure 5. Compressive strenght versus equilibrium density of LWC.

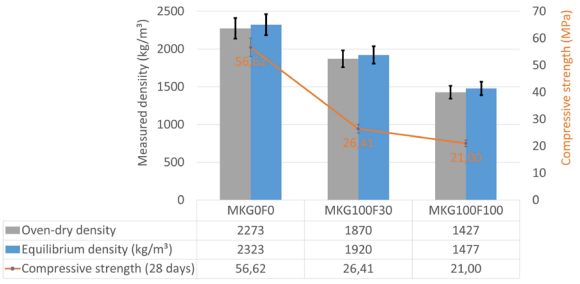

Figure 6. Compressive strenght and equilibrium density of LWC with MK.

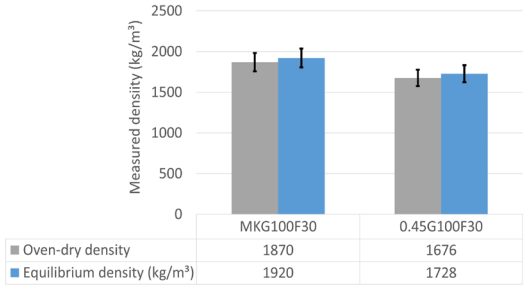

Figure 7. Compressive strenght and equilibrium density of LWC.

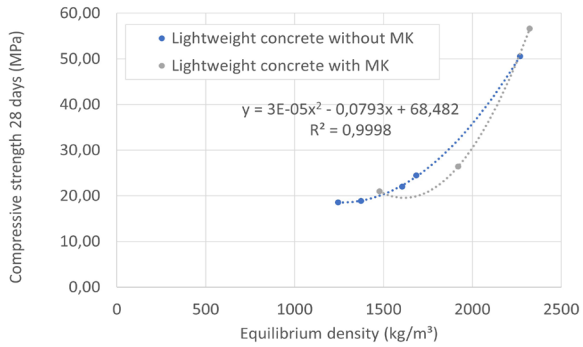

Figure 8. Compressive strenght and density of LWC.

3.2. Physical sulfate attack resistance

At the end of 90 cycles, a negative mass change of 3%–10% was observed for both the NWC and LWC samples (Figure 9). The measured mass changes constituted the mass loss caused by PSA and the mass gain due to extended water exposition, as evidenced for the control sample, G0F0-1, and the formation of new substances inside the samples, in addition to other causes. The results obtained for the concrete bars using the modified ZH90 method were lower than the previously obtained values for normal-weight mortar, even with a low *w/cm* ratio of 0.4 (17). Furthermore, the mass change of the tested samples started by cycle 50 for both NWC and LWC (Figure 9), exhibiting surface scaling, spalling, and flacking. In this PSA test, an incubation period, in which minor damages were observed, was followed by an accelerated mass change, regardless of the use of NWA or TECA. This results in outcomes is similar to the salt scaling observed when tested via freeze and thaw–cycle methods, as depicted in Figure 9. The PSA resistance of LWC exhibiting an improved paste performance owing to the use of MK was higher than that of NWC, demonstrating mass changes of 0.75% and 6.17% for MKG100F30 and G100F30, respectively (Figure 10). The extreme cases among all the TECA samples, namely, G100F100 and MKG100F100, emphasize the substantial effects of paste improvement on the PSA resistance. When a low *w/cm* ratio was used, the mass change decreased from 6.17% to 1.32% in the case of the G100F30 and 0.45G100F30 samples, respectively (Figure 10). This improvement is attributed to the reduced open porosity in the cement paste and pore sizes that positively modified the hydraulic conductivity, ion diffusion, and ion availability to form sodium sulfate crystals. The mass change is primarily affected by the type of binder and the use of SCMs (10). The mass increase observed for the control sample, G0F0-1, devoid of PSA, can be explained by its long-term water exposure that enabled water to penetrate the substantially small and poorly interconnected pores.

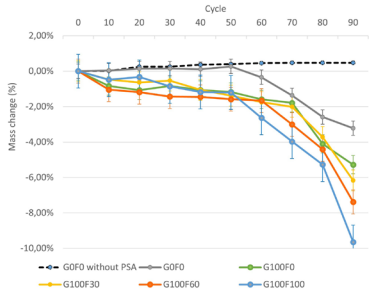

Figure 9. Mass change in the LWC samples subjected to the PSA test.

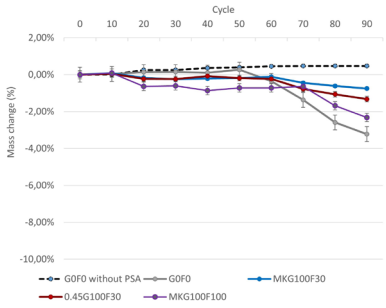

Figure 10. Mass change in the LWC samples with an improved paste performances.

3.3. Visual observations

Figures 11 and 12 depict the damage due to the PSA test for the samples without and with paste improvement, respectively. For comparison, column A presents the data for the unattacked samples maintained in deionized water, whereas column B provides the visual appearance change due to PSA after 90 thermal cycles. Attention must be focused on surface damages, as several end borders had been intentionally broken to obtain the samples for microscopy and XRD analyses. A noticeable difference in damage extension could be perceived by the naked eye, as the samples without paste improvement exhibited more severe surface damage than those with paste improvement. After the PSA test, the samples with paste improvement preserved the characteristics of cycle 0, exhibiting a superficial cement paste skin. The samples without paste improvement demonstrated no noticeable difference in terms of the surface damage regardless of TECA substitutions, although the samples with TECA exhibited certain differences in the mass change.

Figure 11. Samples without paste improvement: Control samples without PSA (A) and damages to the PSA test (B).

Figure 12. Improved cement paste: Control samples without PSA (A), and damage due to the PSA test (B).

The G0F0, G100F30, MKG100F30, and 045G100F30 samples were observed using a microscope (OLYMPUS 8Zx18). This study aimed to identify the damages, visual changes in the pore structure, aggregate conditions, and paste deterioration. The G0F0 sample exhibited scaling on all the surfaces. Several superficial areas comprise exposed aggregates, as depicted in Figure 13(A). Additionally, several small pores were observed (red arrows). As presented in Figure 13(B), the G100F30 sample depicts surface scaling over a substantial area on the surface, and several flakes are on the verge of detachment. A higher number of pores compared to G0F0 were observed, with diameters of approximately <200 µm (red arrow). Additionally, scaling was observed in both the paste and TECA, losing its surface coating, which indicated severe deterioration.

Figure 13.G0F0 (A), and G100F30 (B) samples after the PSA test. Details on the exposed aggregate (Ea), cracks (cr), and scaling (sc) are presented, and red arrows indicate pores.

Figure 14 (A and B) depict the condition of LWC with MK after exposure to PSA. Partial scaling, a low relative porosity (red arrows), and less damage in TECA were observed. However, in certain areas, the TECA particles were exposed owing to severe scaling, indicating mild deterioration. This confirms the differences in the mass change due to the exposure during the PSA test compared to concrete without MK. From Figure 14(C and D), for the 0.45G100F30 sample, scaling is observed over the entire specimen surface, and a certain portion of TECA and pores are exposed, indicating moderate deterioration. The visual inspection suggests that the lower *w/cm* ratio mitigates the PSA damage but does not completely prevent it (18, 25).

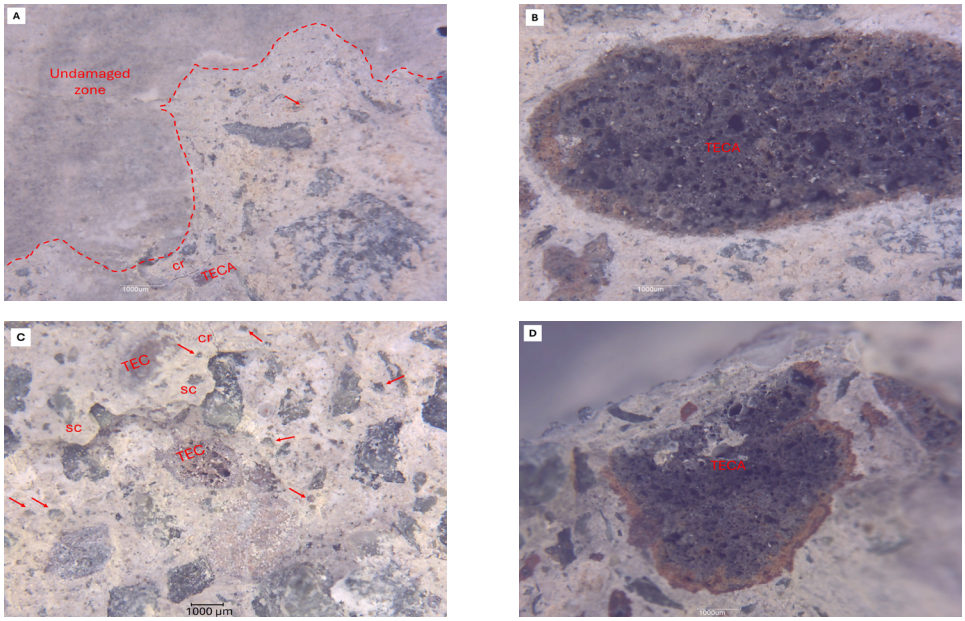

Figure 14. MKG100F30 sample after the PSA test (A), MKG100F30 sample after the PSA test with exposed TECA (B), 0.45G100F30 sample after the PSA test (C), and 0.45G100F30 sample after the PSA test with exposed TECA (D). Details on the exposed aggregate (Ea), cracks (cr), and scaling (sc) are presented, and red arrows indicate the pores.

3.4. Open porosity and hydraulic conductivity

The relations between the open porosity and hydraulic conductivity with the mass change are depicted in Figures 15 and 16. For the samples with an improved paste performance, namely, MKG100F30 and 0.45G100F30, the open porosity and penetration depth were similar to those of G0F0, suggesting that both the methods for paste improvement effectively contribute to weaken the transport mechanisms. The higher open porosity and hydraulic conductivity of G100F30 resulted in a larger mass change due to PSA. Furthermore, similar hydraulic conductivity and porosity values observed for G0F0, MKG100F30, and 0.45G100F30 resulted in similar mass changes.

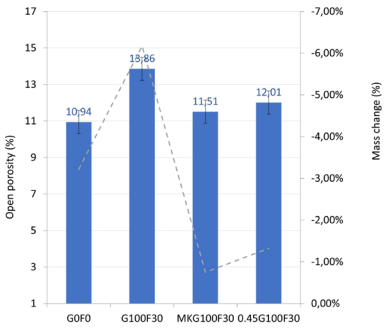

Figure 15. Relation between the open porosity and mass change.

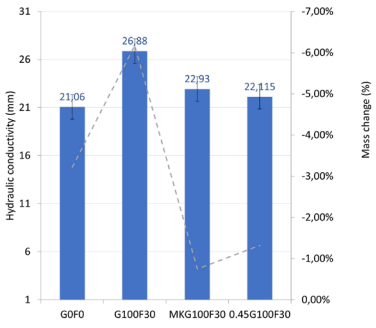

Figure 16. Relative performance to the water pentration depth.

3.5. Absorption

Different from hydraulic conductivity, under a pressure gradient, sorptivity reflects the volume of water absorbed via capillary action in an exposed area. Figure 17 depicts the results of sorptivity analysis. The initial sorptivity values are similar for NWC and LWC; however, during late absorption, approximately after 150 $s^{0.5}$, certain differences are observed. F0G0 exhibited the highest late or secondary sorptivity, which was similar to that of G100F30. TECA does not appear to modify the water-transportation properties of the concrete. As a paste-improvement method, the use of MK to reduce sorptivity was relatively more effective than decreasing the *w/cm* ratio. The results assert that absorption depends on the properties of the cementitious paste, as observed in the cases of hydraulic conductivity and water penetration depth, and modifies the transport mechanisms. These findings are similar to those of other studies that predicted the capillary rise heights of the PSA solution based on an absorption model for concretes with different *w/cm* ratios, suggesting that the changes in the sub-efflorescence heights due to the variations in the *w/cm* ratio were negligible (10). Notably, all the samples were saturated after curing, including those cured in water before PSA, and therefore, the prevailing ingress mechanism during the PSA test was diffusion.

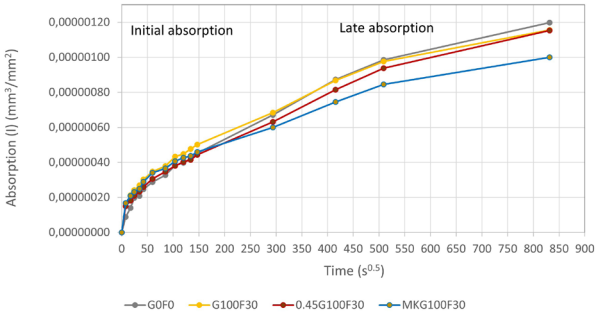

Figure 17. Concrete absorption..

3.5. Scanning Electron Microscope observations

After the PSA test, selected samples were analyzed using SEM. The samples were obtained from the flakes on the surface of the specimens. In G0F0, pinacoidal formations and twinning are observed, as depicted in Figure 18(B). EDS analysis identified the presence of Ca (88.7%), along with the traces of sodium sulfate. Additionally, Figure 18(C) indicates the presence of gypsum exhibiting a prismatic morphology, which is attributed to the chemical reaction between sodium sulfate and portlandite.

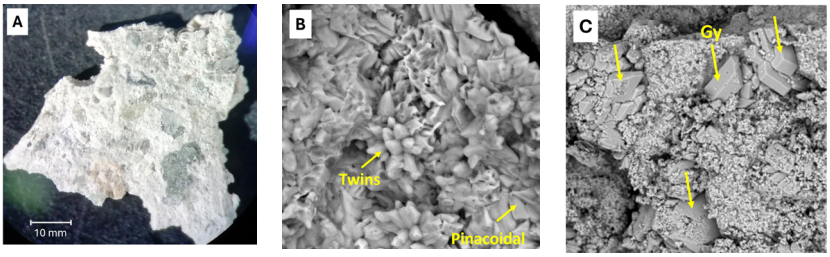

Figure 18. G0F0 sample: Flake after PSA attack (A), gypsum and several sodium sulfate crystals (B), and gypsum detail (Gy) (C).

The G100F30 LWC sample possessed pores in the paste matrix, with their diameters ranging from 27.28 to 121.6 µm (Figure 19(C)) and an ITZ with a higher degree of densification, figure 19(D), than that in G0F0. This might be due to the reaction of aluminosilicates, which were present in amorphous TECA, with CH, leading to an ITZ with a higher degree of formation of C–S–H and C–A–S–H, as reported elsewhere (18). The latter enabled the refinement of pores, altered the ITZ, reduced the space for the formation of sodium sulfate crystals and other substances, and changed the transport mechanisms (Figure 19(B)). However, in several sectors of the ITZ (Figure 19(E)), the presence of structures with acicular and fibrous crystalline characteristics were observed, which were identified as thaumasite via EDS. Furthermore, Figure 19(F) depicts dendritic morphologies, indicating the presence of thenardite, which has been confirmed via EDS, possessing a micrometric size that pseudomorphically replaces mirabilite after its dehydration (26). Notably, the sodium sulfate phases observed in the SEM analysis might have been previously altered because of environmental exposition and high-vacuum conditions during the microscopic analysis. Additionally, ettringite was detected in the paste region (Figure 19(G)), as a result of the presence of water and sulfates.

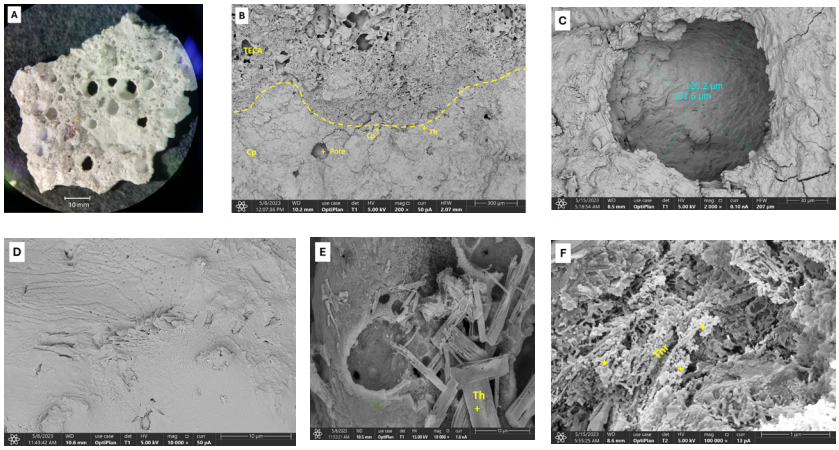

Figure 19. G100F30 sample: Porous flake obtained after the PSA test (A), cement paste (Cp) and TECA morphologies (B), pore in the cement paste matrix (C), ITZ in detail (D), details of thaumasite (Th) on the TECA surface (E), dendritic appearance of thenardite (Thr) (light gray) (D), and ettringite (Et) (G).

The MKG100F30 sample comprises a structure with a relatively higher degree of pore refinement compared to G100F30, as observed in Figure 20(B and F). Furthermore, the C–S–H gel was observed in a considerable portion of the cementitious paste, and the traces of sodium sulfate were detected via EDS. Figure 20(C and D) reveal the presence of a scarce amount of substances with a morphology comparable with that of thenardite and localized on the failure surface of the sample. Figure 20(E) depicts a pore with a diameter of 26.78 µm in the cementitious paste, along with the presence of a large amount of gypsum based on the morphology and EDS analyses. Inside the TECA pores, no sodium sulfate crystals or other foreign substances are detected, as demonstrated in Figure 20(B and G).

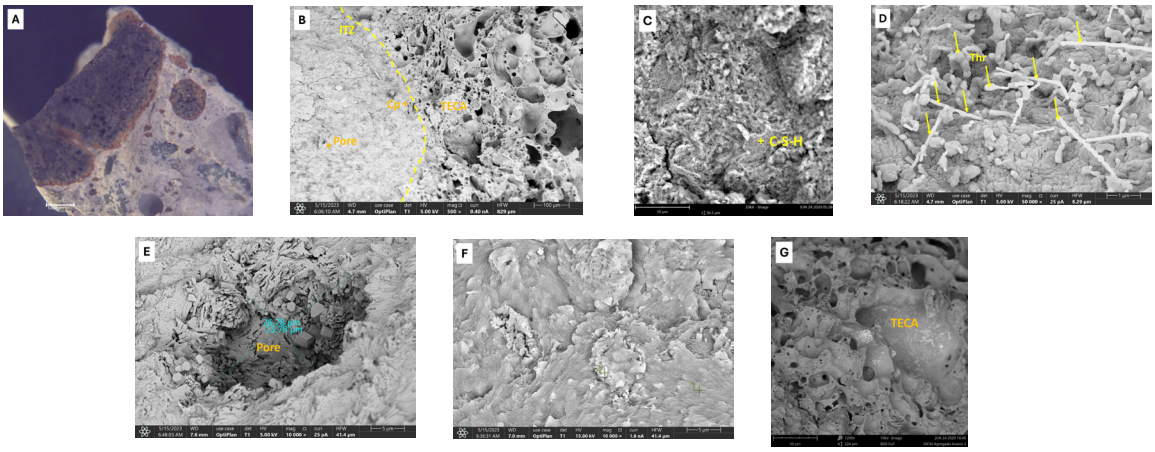

Figure 20. MKG100F30 sample: Damage after the PSA test (A), details of cementitious paste (Cp) and TECA (B), C–S–H gel (C). Thenardite (Thr) (D), pore in cementitious paste (E), ITZ details (F), and details of the TECA alveolar structure without foreign substances (G).

Figure 21 presents the data for the 0.45G100F30 sample. Figure 21(B) depicts a pore with a diameter of 161.3 µm and whose surface is partially coated with indistinct crystallites. Furthermore, the ITZ structure is illustrated. The alveolar structure of TECA indicates the absence of foreign substances. Figure 21(C) reveals the presence of a large amount of gypsum owing to the chemical reactions of the cement paste with the sulfate solution. From Figure 21(D), the C–S–H can be identified through its morphology, and its presence is confirmed via EDS. Furthermore, it is inferred the C–S–H to contain thenardite based on its composition determined via EDS, revealing sodium and sulfur contents of 4.96% and 2.39%, respectively. Ettringite is identified through its morphology, and its presence is further confirmed via EDS analysis, as illustrated in Figure 21(E).

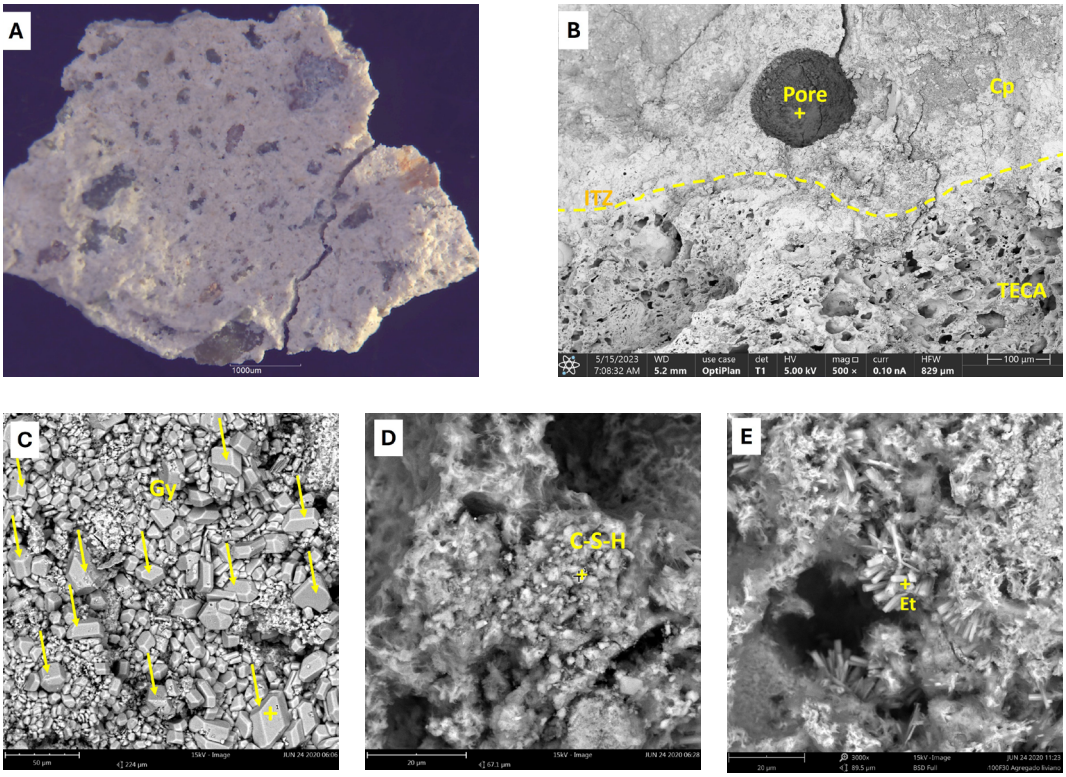

Figure 21. 0.45G100F30 sample: damage after the PSA test (A), cement paste (Cp) – TECA (B), gypsum (Gy) (C), C–S–H (D) and Ettringite (Et) (E).

3.6. X-Ray Diffraction results

To confirm the findings obtained via SEM, XRD analysis was conducted, and the results are presented in Figures 22 and 23. Portlandite (Prt), ettringite (Et), and gypsum (Gy) were detected in all the samples. Additionally, quartz (Q), calcite (Ca), plagioclase (P), and clinochlore (Chl) were present, which was attributed to the minerals in the aggregates. From Figure 23, gypsum, ettringite, and thenardite can be identified. The green arrows indicate thenardite (Thr). Mirabilite was not detected. As previously mentioned, changes in the environmental conditions, such as relative humidity, temperature, and vacuum, may modify the sodium sulfate phases in the samples, and therefore, their presence does not confirm the occurrence of crystallization and recrystallization during the PSA test (25). The semiquantitative XRD results presented in Table 5 reveal that a larger quantity of gypsum and ettringite, together amounting to approximately 11%, is present in G100F30, which corresponds to the larger mass change observed during PSA. For MKG100F30, the overall content of gypsum and ettringite was 4%–9%.

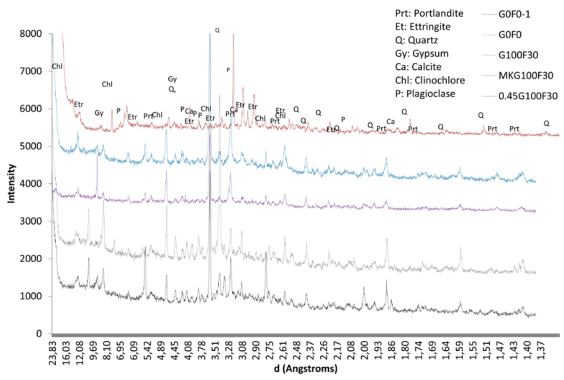

Figure 22. Diffractograms of the samples.

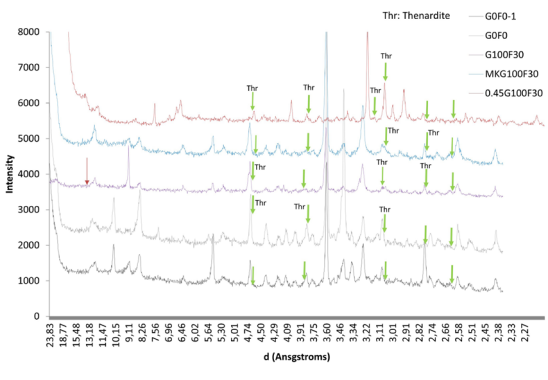

Figure 23. Identification of the thenardite via XRD.

Table 5. Semiquantitative XRD results for the mineral identification of concrete samples.

Mineral	G0F0-1 Control	G0F0	G100F30	MKG100F30	0.45G100F30
Quartz	22 to 27%	35 to 40%	18 to 22%	33 to 38%	20 to 24%
Portlandite	3 to 7%	< 3%	< 3%	< 3%	< 4%
Ettringite	< 5%	< 4%	< 6%	3 to 8%	< 5%
Gypsum	< 1%	< 2%	< 5%	< 1%	< 2%
Calcite	< 5%	< 4%	3 to 7%	< 5%	3 to 7%
Clinochlore	5 to 10%	5 to 10%	3 to 8%	3 to 8%	8 to 12%
Plagioclase	5 to 10%	5 to 10%	5 to 10%	5 to 10%	8 to 12%
Others/ amorphous	40 to 45%	30 to 35%	40 to 45%	30 to 5%	38 to 43%

The presence of thaumasite detected via XRD and SEM leads to the conclusion that a dual sulfate attack occurs during the PSA tests. Furthermore, the occurrence of a dual attack has been reported by Neville and other authors (1, 27, 28). This implies that the negative mass change observed for the modified ZH90 method cannot solely be attributed to pure PSA, i.e., due to the crystallization and recrystallization of sodium sulfate. The temperature ranges adopted in the modified ZH90 method may not promote the phase changes between thenardite and mirabilite; however, the crystallization kinetics may facilitate the aforementioned crystallization and recrystallization processes.

4. CONCLUSIONS

The use of the modified ZH90 method for assessing the PSA resistance of LWC resulted in chemical and physical attacks, i.e., a dual attack that explained the negative mass loss via surface scaling. The presence of gypsum, thaumasite, and a certain amount of ettringite confirms the occurrence of a chemical reaction with the sulfates and cementitious compounds. Thenardite was detected via XRD and SEM analyses and was associated with PSA. This method does not facilitate the differentiation of the corresponding individual contributions to the chemical and physical damage.

LWC composed of TECA exhibited an increased relative mass change during the PSA tests with respect to NWC. A high degree of replacement of NWA by TECA resulted in a decrease in the compressive strength and an increase in the negative mass change. These results imply that in the absence of other measures, when the concrete density was reduced, the PSA crystallization pressure could easily overpass the concrete strength. However, this behavior could easily be reversed with paste improvement, such as by decreasing the *w/cm* ratio or using MK, with no further increments in the cementitious content to increase the compressive strength. The transport mechanisms of the sodium sulfate solution were relatively similar for LWC and NWC, as the values of the hydraulic conductivity, sorptivity, and open porosity were similar, even when NWA was completely replaced by TECA. These study findings may guide the use of LWC in sulfate-rich environments.

Authorship contribution statement

Paula A. Lopez: Conceptualization, Methodology, Research; Writing – original draft.

Jorge I. Tobón: Writing – review & editing, Conceptualization; Methodology, Supervision.

Juan F. Arango-L: Writing – review & editing, Conceptualization, Methodology; Supervision.

Declaration of competing interest

The authors of this article declare that they have no financial, professional or personal conflicts of in-terest that could have inappropriately influenced this work.

REFERENCES

1. Neville A. 2011. Properties of concrete. Canada: Pearson.
2. Shan ZQ, Yin GJ, Wen XD, Miao L, Wang SS, Zuo XB. 2024. Numerical simulation on transport-crystallization-mechanical behavior in concrete structure under external sulfate attack and wetting–drying cycles. Mater. Des. 241:112908.

https://doi.org/10.1016/j.matdes.2024.112908
3. Omrani IAN, Waldemar M, Świątkowski M. 2024. Role of climatic cycles on the duality of chemical and physical modes of sulfate attack in concrete. J. Civ. Eng. Constr. 13(3):146-158. https://doi.org/10.32732/jcec.2024.13.3.146
4. Suleiman A, Nehdi ML. 2016. Effect of pore structure on concrete deterioration by physical sulphate attack. Resilient infrastructure (conference). https://www.researchgate.net/publication/313756523
5. Nadelman EI, Kurtis KE. 2019. Durability of Portland-limestone cement-based materials to physical salt attack. Cem. Concr. Res. 125:105859. https://doi.org/10.1016/j.cemconres.2019.105859
6. Tobón JI, Payá J, Restrepo O. 2015. Study of durability of Portland cement mortars blended with silica nanoparticles. Constr. Build. Mater. 80:92-97. https://doi.org/10.1016/j.conbuildmat.2014.12.074
7. Nehdi ML, Suleiman AR, Soliman AM. 2014. Investigation of concrete exposed to dual sulfate attack. Cem. Concr. Res. 64:42-53. https://doi.org/10.1016/j.cemconres.2014.06.002
8. Zhutovsky S, Hooton RD. 2016. Evaluation of concrete's resistance to physical sulfate salt attack. International RILEM Conference on Materials, Systems and Structures in Civil Engineering Conference segment on Service Life of Cement-based Materials and Structures 22-24 August 2016, Technical University of Denmark, Lyngby, Denmark. https://www.researchgate.net/publication/306960534
9. Esselami R, William W, Tagnit-Hamou A. 2022. An accelerated physical sulfate attack test using an induction period and heat drying: First applications to concrete with different binders including ground glass pozzolan and limestone filler. Construction and Building Materials, Vol. 345, p. 128046. https://doi.org/10.1016/j.conbuildmat.2022.128046
10. Najjar MF, Nehdi ML, Soliman AM, Azabi TM. 2017. Damage mechanisms of two-stage concrete exposed to chemical and physical sulfate attack. Constr. Build. Mater. 137:141-152. https://doi.org/10.1016/j.conbuildmat.2017.01.112
11. Deng G, He Y, Lu L, Wang F, Hu S. 2022. Investigation of sulfate attack on aluminum phases in cement-metakaolin paste. J. Build. Eng. 56:104720. https://doi.org/10.1016/j.jobe.2022.104720
12. Zhutovsky S, Hooton D. 2016. Effect of supplementary cementitious materials on the resistance of mortar to physical sulfate salt attack. Conference: 5th International Materials Specialty Conference, Annual Conference of Canadian Society for Civil Engineering. London, Ontario, Canada. https://www.researchgate.net/publication/306077939
13. Ding W, He Y, Lu L, Wang F, Hu S. 2021. Mechanical property and microstructure of quaternary phase paste blended with metakaolin. Cem. Concr. Compos. 118:103934. https://doi.org/10.1016/j.cemconcomp.2021.103934
14. American Concrete Institute ACI 201.2R-16. 2016. Guide to durable concrete. U.S.A.
15. Alyami MH, Alrashidi RS, Mosavi H, Almarshoud MA, Riding KA. 2019. Potential accelerated test methods for physical sulfate attack on concrete. Constr. Build. Mater. 229:116920. https://doi.org/10.1016/j.conbuildmat.2019.116920
16. Drimalas T. 2007. Laboratory and field evaluations of external sulfate attack (dissertation). Texas: S.N. http://hdl.handle.net/2152/3569
17. Zhutovsky S, Hooton RD. 2017. Experimental study on physical sulfate salt attack. Materials and Structures. 50:54. https://doi.org/10.1617/s11527-016-0936-z
18. Vargas P, Restrepo Oscar, Tobón JI. 2017. Microstructural analysis of interfacial transition zone (ITZ) and its impact on the compressive strength of lightweight concretes. Constr. Build. Mater. 137:381-389. https://doi.org/10.1016/j.conbuildmat.2017.01.101
19. Vargas P, Marín NA, Tobón, JI. 2018. Performance and microstructural analysis of lightweight concrete blended with nanosilica under sulfate attack. Adv. Civ. Eng. 2018(1):2715474. https://doi.org/10.1155/2018/2715474
20. Zhutovsky, Hooton RD. 2017. Accelerated testing of cementitious materials for resistance to physical sulfate attack. Constr. Build. Mater. 145:98-106. https://doi.org/10.1016/j.conbuildmat.2017.03.239
21. Sakr MR, Bassuoni MT, Hooton RD, Drimalas T, Haynes H, Folliard KJ. et al. 2020. Physical salt attack on concrete: Mechanisms, influential factors, and protection. ACI Mater. J. 29:253-268. http://doi.org/10.14359/51727015
22. Abiev R, Kozlov VV. 2018. Study of properties of foam concrete produced by means of vortex jet apparatus. Bulletin of the Saint Petersburg State Institute of Technology, 43:71-76. https://doi.org/10.15217/issn1998984-9.2018.43.71
23. Kozłowski M, Kadela M. 2018. Mechanical characterization of lightweight foamed concrete. Advances in Materials Science and Engineering. Hindawi Publishing, 2018(1):6801258. https://doi.org/10.1155/2018/6801258
24. Samson G, Phelipot-Mardelé A, Lanos, C. 2017. A review of thermomechanical properties of lightweight concrete. Mag. Concr. Res. 69(4):201-216. https://doi.org/10.1680/jmacr.16.00324
25. Rodriguez C, Doehne E, Sebastian E. 2000. How does sodium sulfate crystallize? Implications for the decay and testing of building materials. Cem. Concr. Res. 30(10):1527-1534. https://doi.org/10.1016/S0008-8846(00)00381-1
26. Neville A. Tecnología del concreto. 2013. Instituto Mexicano del Cemento y del Concreto, A.C.
27. Liu P, Chen Y, Wang W, Yu Z. 2020. Effect of physical and chemical sulfate attack on performance degradation of concrete under different conditions. Chem. Phys. Lett. 745:137254. https://doi.org/10.1016/j.cplett.2020.137254
28. Bassuoni MT, Rahman M. 2016. Response of concrete to accelerated physical salt attack exposure. Cem. Concr. Res.79:395-408. https://doi.org/10.1016/j.cemconres.2015.02.006